which should be cited to refer to this work.

Depth profiling of low energy ion implantations in Si and Ge by means of micro-focused grazing emission X-ray fluorescence and grazing incidence X-ray fluorescence

Yves Kayser,*[ab] Philipp Hönicke,[c] Dariusz Banaś,[d] Jean-Claude Dousse,[a] Joanna Hoszowska,[a] Paweł Jagodziński,[e] Aldona Kubala-Kukuś,[d] Stanisław H. Nowak†[a] and Marek Pajek[d]

Depth-profiling measurements by means of synchrotron radiation based grazing XRF techniques, *i.e.,* grazing emission X-ray fluorescence (GEXRF) and grazing incidence X-ray fluorescence (GIXRF), present a promising approach for the non-destructive, sub-nanometer scale precision characterization of ultra shallow ion-implantations. The nanometer resolution is of importance with respect to actual semiconductor applications where the down-scaling of the device dimensions requires the doping of shallower depth ranges. The depth distributions of implanted ions can be deduced from the intensity dependence of the detected X-ray fluorescence (XRF) signal from the dopant atoms on either the grazing emission angle of the emitted X-rays (GEXRF), or the grazing incidence angle of the incident X-rays (GIXRF). The investigated sample depth depends on the grazing angle and can be varied from a few to several hundred nanometers. The GEXRF setup was equipped with a focusing polycapillary half-lens to allow for laterally resolved studies. The dopant depth distribution of the investigated low-energy (energy range from 1 keV up to 8 keV) P, In and Sb ion-implantations in Si or Ge wafers were reconstructed from the GEXRF data by using two different approaches, one with and one without *a priori* knowledge about the bell-shaped dopant depth distribution function. The results were compared to simulations and the trends predicted by theory were found to be well reproduced. The experimental GEXRF findings were moreover verified for selected samples by GIXRF.

1 Introduction

The physical, chemical and electrical properties of semiconductor materials can be modified by means of various doping techniques like diffusion or ion implantation. The goal is to tailor the properties of the sample volume affected by the doping process in order to realize specific applications and to improve the performances of the produced devices. Recent advances were essentially realized by down-scaling the device size since this allows for increased device speed and integrated circuit complexity. Furthermore the power consumption and cost of the individual units are reduced. To preserve a constant aspect ratio when down-sizing, the depth region to be doped has to be scaled with the device size and becomes therefore also shallower. Moreover, the short-channel effect, which implies increased leakage currents, thus a limited device performance, can be suppressed by designing devices based on USJ (ultra-shallow junctions) with junction depths of only several tens of nanometers.

Among the available doping techniques ion implantation presents the best control over the relevant parameters (dopant atoms, implantation energy and dose) for the final dopant distribution (laterally to the surface and in the depth direction), a great flexibility (possible material combinations, sequential doping of the same wafer) as well as an excellent reproducibility.[1,2] The distribution of the implanted ions is characterized by a maximum concentration peak with tails on both sides of the concentration peak. The latter are due to the random nature of the (electronic and nuclear) collisions of the dopant ions with the substrate atoms during the implantation process. Therefore the energy loss in each collision is a stochastic process. The depth distribution is in general best described by a Pearson IV distribution.[3] In order to produce the ultra-shallow dopant profiles required for semiconductor applications, the

[a]*Department of Physics, University of Fribourg, 1700 Fribourg, Switzerland. E-mail: yves.kayser@psi.ch; Tel: +41 56 310 3555*

[b]*Paul Scherrer Institut, 5232 Villigen-PSI, Switzerland*

[c]*Physikalisch-Technische Bundesanstalt, 10587 Berlin, Germany*

[d]*Institute of Physics, Jan Kochanowski University, 25-406 Kielce, Poland*

[e]*Department of Physics, Kielce University of Technology, 25-314 Kielce, Poland*

† Present address: IfG – Institute for Scientific Instruments GmbH, Berlin, Germany.

implantation energies are decreased to a few keV at the expense of the maximum beam current. Alternatively, for a given implantation energy, shallower profiles can be produced in a Ge matrix compared to a Si matrix because of the higher Ge density. Despite the smaller band gap resulting in a higher sensitivity to short-channel effects and the lack of a stable oxide needed for surface passivation and etch protection, Ge draws again an increased interest because of physical limitations of Si in the down-scaling of device dimensions, attractive electrical and chemical properties (ability to deposit high-k gate dielectrics, high mobility of electrons and holes) and recent significant advances towards the industrial use of Ge.[4–11]

An accurate experimental assessment of the dopant depth concentration profiles is quite challenging but mandatory in order to characterize the implantation (and also the annealing) techniques and to support further technical advances in the semiconductor industry. Channeling and (transient enhanced) diffusion make a theoretical prediction of the dopant distribution difficult. The trend of shrinking down device sizes to some nanometers requires a reliable and precise characterization of dopant depth distributions in semiconductor materials. Novel and improved diagnostic tools for the experimental profiling of dopants in semiconductor materials on a depth scale of about 20 nm or even less and the determination of the retained dose are essential and called for.

Depth-profiling measurements in the vicinity of the surface can be realized by means of different techniques like for example time-of-flight secondary ion mass spectroscopy (TOF-SIMS),[12] Rutherford backscattering (RBS),[13] medium energy ion scattering (MEIS),[14] elastic recoil detection analysis[15] or total reflection X-ray fluorescence (TXRF) combined with sputtering.[16] Each of the mentioned methods has its merits and inherent limitations in terms of sample consumption, cost of analysis, quantification, chemical and elemental sensitivity, lateral and depth resolution, and accessible depth region. Often a combination of the different techniques is used to gather the required information.[17] Comparisons of different surface-sensitive analytical techniques can be found in the literature.[18–21]

2 Depth profiling by means of grazing XRF techniques

With respect to the above mentioned techniques, X-ray based approaches are non-destructive and do not necessarily require a high-vacuum environment like it is the case for particle-based methods. Furthermore no sample preparation is required, a wide range of materials regarding the elemental and chemical composition as well as the concentration (implantation dose for ion-implanted samples) can be studied. Quantitative measurements can be performed if either a calibration sample is used or the measurements are performed with calibrated instrumentation.[22] If the X-ray fluorescence (XRF) measurements are realized in a grazing geometry (Fig. 1, left panels), *i.e.*, either in the grazing emission X-ray fluorescence[23–26] (GEXRF) or in the grazing incidence X-ray fluorescence[27–31] (GIXRF) configuration,

a high sensitivity with respect to the surface-near sample composition can be achieved. Combinations of the grazing incidence and emission geometries were also realized in the past in order to profit simultaneously from the surface sensitivity of both techniques. To better control the depth range which is explored in the sample both grazing angles are varied, resulting in exhaustive datasets.[32–36] The surface sensitive character of GEXRF and GIXRF was profited from to detect trace amounts of impurities on or inside wafers.[37–44] In the context of surface analysis on a nanometer scale, the disadvantage of the large penetration range of X-ray radiation compared to (charged) particles is circumvented by detecting the emitted intensity of a single or multiple characteristic XRF lines at well-defined grazing emission angles (Fig. 1, bottom left panel) or by irradiating the sample surface with monochromatic X-rays at well-defined grazing incidence angles (Fig. 1, top left panel). The probed depth region can be tuned with the grazing angle from a few nanometers up to several hundreds of nanometers and depends on the X-ray energy of interest and the sample matrix. For identical X-ray energies of interest, the depth distribution of the atoms contributing at a given grazing angle to the observable XRF yield does not depend on the grazing geometry. Indeed, through the principle of microscopic reversibility it can be concluded that the grazing emission and the grazing incidence geometry are physically equivalent.[26,45] The X-ray energy of interest is, however, in the grazing emission geometry the one of the monitored characteristic XRF line(s) and in the grazing incidence geometry the one of the incident radiation used for the excitation of the XRF signal (Fig. 1, right panel). The angle-dependent depth ranges are well suited to characterize the distributions of ions resulting from implantations realized with energies in the (lower) keV-regime where the typical ion penetration ranges are on the scale of several tens of nanometers to at most hundreds of nanometers. The tunability of the probed depth region with the grazing angle in combination with the linearity in the intensity response of X-ray detectors was already applied to depth-profiling measurements of ion-implanted samples (Al, As and B dopants in Si wafers were considered) by means of GEXRF and GIXRF.[46–51] It has to be pointed out that for the reported dopant–wafer combinations, the measurements could be performed either with excitation energies below the Si K-edge (1839 eV), thus avoiding a significant background contribution from the wafer material or at energies above the As K-edge (11867 eV). In the latter situation the Si absorption cross-section is small and the As XRF signal can be well separated from the Si $K\alpha$ line. In the present study different dopant wafer combinations, namely P, In and Sb in Si and P implantations in Ge, with technologically relevant implantation fluences were investigated with a special focus on the sub-20 nm depth range and using for the first time a synchrotron-radiation based micro-focused high-energy resolution GEXRF setup. Moreover selected samples were also investigated by means of GIXRF. In contrast to the previously investigated ion-implanted samples with a GEXRF or GIXRF setup, the measurements for the samples considered hereafter had to be performed with incident beam energies above the Si K edge, resp. Ge L_3 edge (1217 eV) because the K and L_3
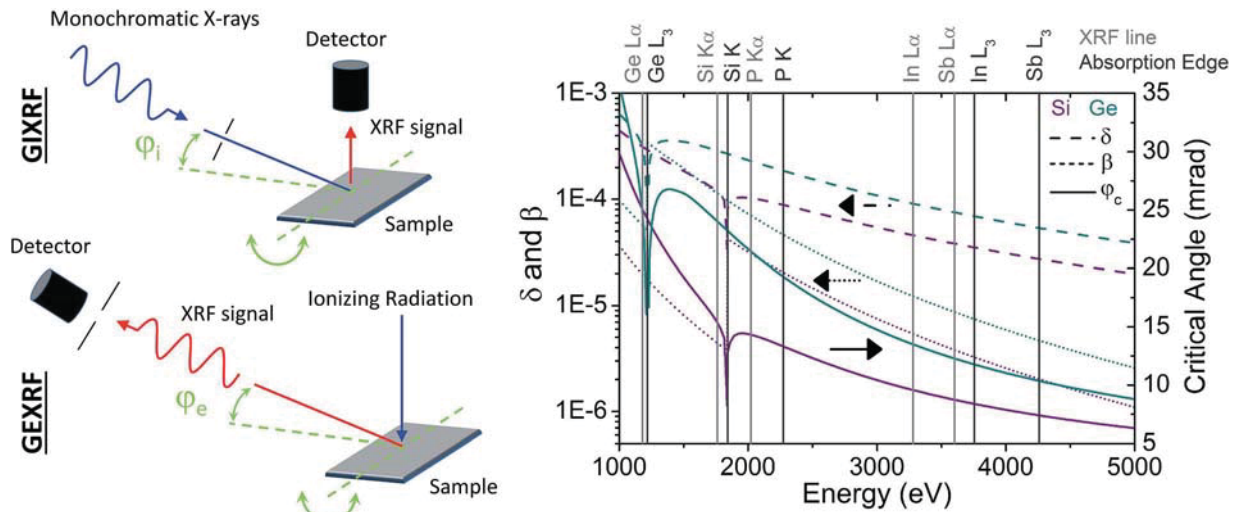
Fig. 1 Illustration of the typical geometry for a grazing incidence (top left panel) and a grazing emission X-ray fluorescence setup (bottom left panel). In both configurations the intensity of the XRF signal is measured as a function of the grazing angle. While in GIXRF monochromatic X-rays have intrinsically to be used for the excitation of the XRF signal, in GEXRF (polychromatic) X-ray or particle beams can be used. The grazing angle has in both geometries to be well-defined with respect to the sample surface plane. From the geometrical configuration it can be recognized that the energy of interest for the calculation of the critical angle of ion-implanted Si and Ge wafers is in GEXRF the energy of the considered characteristic XRF line(s) and in GIXRF the energy of the incident beam. The latter has to be above the elemental absorption edge of the XRF line which is to be measured.

absorptions edges of the investigated dopant elements are higher in energy. It will be shown that despite more challenging experimental conditions (background contributions from the wafer matrix because of incident beam energies closer to the Si K edge, resp. Ge L$_3$ edge), the used GEXRF and GIXRF setups proved to be suitable for the depth-profiling of the various dopant concentration distributions.

In a GEXRF setup the grazing emission angle is defined as the angle subtended between the sample surface and the observation direction to which the detection setup is sensitive (Fig. 1, bottom left panel). The latter can either be an energy-dispersive detector associated to a slit system for reasons of angular resolution or a wavelength dispersive setup. In the latter case the discrimination of the grazing emission angles is realized with the dispersive element.[23] The dependence of the XRF intensity on the grazing emission angle is usually measured sequentially by changing successively the sample-detection setup orientation, either the sample or the detector position being scanned. Alternatively a position-sensitive area detector allows, by dispersing the grazing emission angle scale along one of the detector dimensions, to acquire the GEXRF intensity profile in a single measurement without scanning successively through different sample-detector orientations as it is required for standard GEXRF setups.[52] In GIXRF the angular intensity profile has also to be measured in a series of sequential measurements. The grazing incidence angle corresponds to the angle between the sample surface and the monochromatic incident X-ray beam used for the excitation of the XRF signal (Fig. 1, top left panel). The incident X-ray beam should be characterized by a low divergence for reasons of angular resolution and the XRF signal is usually detected by means of an energy-dispersive detector mounted close to the

sample surface in order to maximize the solid angle of detection. In order to have well-defined grazing angles the sample surface needs to be optically flat and smooth and since the critical angle for total external reflection depends on the incident X-ray energy a monochromatic X-ray beam is required. The angular range to be covered in grazing XRF experiments extends from 0 mrad to angles larger than twice the critical angle φ_c for total external reflection. The latter depends on the sample matrix and inversely on the X-ray energy of interest (Fig. 1, right panel). Thus, for ion-implanted samples, the critical angle when observing the XRF signal of the dopants will in general be smaller in the grazing incidence geometry and the probed depth range at a give grazing angle will be slightly different (Fig. 1, right panel). Moreover possible interference fringes in grazing XRF intensity profiles usually observed in the analysis of layered samples by means of GEXRF,[23,53–55] respectively GIXRF,[56–59] will appear at different angular positions. Interference fringes can also be observed for artificial nanostructures on the top of a substrate in the GEXRF and GIXRF intensity profiles.[60–62] Note, that for the considered ion-implanted samples no interference fringes will show up in the angular intensity profiles since there is only one refraction interface for the incident, respectively emitted X-rays (the sample surface itself) and since the XRF signal originates from below the refracting interface. A further experimental difference between GIXRF and GEXRF is given by a different sensitivity of the sample matrix to the respective X-ray energy of interest, the difference being pronounced by the long emission, respectively incidence paths.

As mentioned the depth-profiling capability of both grazing XRF geometries is given by the possibility to tune the probed depth region by varying the grazing angle at which the fluorescence signal is detected (GEXRF), respectively excited
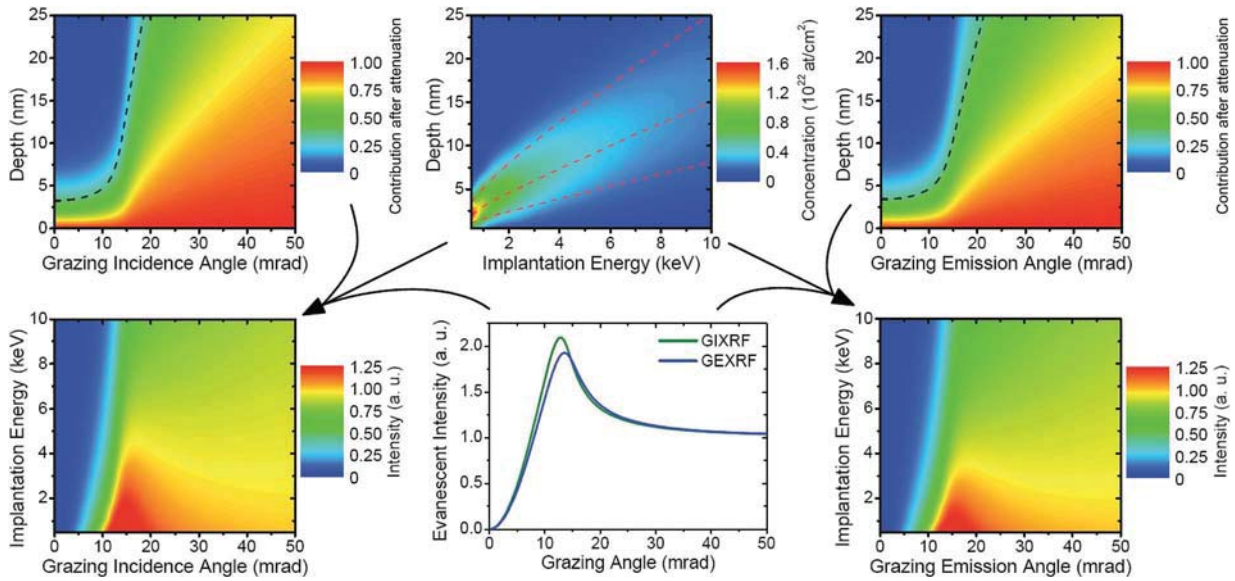
Fig. 2 Illustration of the application of GIXRF and GEXRF towards the characterization of the dopant depth distribution of P-implanted Si wafers. The SRIM simulation allows to represent the depth distribution of the dopants as a function of the implantation energy (top middle panel). The middle dashed line indicates the depth position of the maximum concentration peak, the top and bottom dashed lines show the standard deviation of the dopant distribution on either side of the concentration peak. With increasing implantation energies the dopant ions penetrate on average deeper into the wafer and spread over a larger region. The pronounced attenuation of the X-rays incident at (top left panel), respectively emitted at a grazing angle (top right panel) with respect to the sample surface allows for depth-profiling measurements by means of GIXRF and GEXRF. The dashed line represents the extinction depth. For GEXRF the energy of the P Kα_1 line was considered and for GIXRF an energy of 2200 eV just above the P K edge. Considering in addition the angle-dependent evanescent intensity (transmittivity, bottom middle panel), the dependence of the XRF intensity on the grazing angle can be calculated (eqn (1), bottom left panel for GIXRF, bottom right panel for GEXRF).

(GIXRF). In Fig. 2 (top right panel for GEXRF, top left panel for GIXRF) the attenuation of the emitted, respectively incident X-ray photons as a function of the sample depth is plotted for the case of a P-implanted Si wafer. In the case of GIXRF an incident photon energy (2200.0 eV) above the P K edge (2145.5 eV) is assumed, whereas in the case of GEXRF the energy of the P Kα_1 (2013.7 eV) is considered. An estimate of the probed depth region at each grazing angle is provided by the corresponding extinction depth (Fig. 2, dashed lines in the top left and right panels). The latter corresponds to the distance measured vertically from the surface for which X-ray photons emitted, respectively incident at the selected grazing angle are attenuated by a factor e^{-1}. The contribution of the P atoms on the attenuation was neglected. Below the respective critical angle, only the first few nanometers can contribute to the detectable XRF signal. Indeed, because of the refraction at the sample surface according to the Fresnel laws and since the sample is the optically less dense medium, in the grazing emission geometry the X-ray photons emitted by bulk atoms can not be observed for grazing emission angles smaller than the critical angle,[25] whereas in the grazing incidence geometry no XRF signal in the bulk can be produced for grazing incidence angles below the critical angle because of total external reflection.[63] In both grazing geometries the contribution of the surface-near volume in the angular range below the critical angle is explained by an evanescent wave with a non-negligible amplitude.[45]

When varying the grazing angle to values above the critical angle, the accessible depth region starts to increase at first significantly, then in a first approximation linearly with the grazing angle (Fig. 2, top left and top right panels). In the grazing emission geometry the XRF signal produced in the bulk starts to contribute to the measured XRF intensity, while in the grazing incidence geometry the excitation of the XRF signal is no longer restricted to the surface-near region. The probed depth volume is essentially limited by the attenuation of the XRF photons (GEXRF), respectively incident X-ray photons (GIXRF).

The grazing angle-dependent depth sensitivity is hereafter exploited for retrieving the depth distribution of the dopant atoms of different ion-implanted samples by measuring the XRF intensity dependence on the grazing angle. As an illustration, the theoretical implantation energy dependent depth concentration distributions of P ions implanted into a Si wafer is shown in Fig. 2 (top middle panel). The theoretical depth profiles were calculated with the SRIM program which is a Monte Carlo simulation of the implantation process taking into account different physical effects.[64] Surface sputtering which can lead to a distortion or broadening of the profile was neglected. For a given ion depth distribution $f(z)$, the dependence of the XRF intensity on the grazing angle $I(\varphi)$ can be calculated (Fig. 2, bottom left and right panels) using the following formula:

$$I(\varphi) \propto \left| \frac{2 \sin \varphi}{\sqrt{n(\lambda)^2 - \cos^2 \varphi} + \sin \varphi} \right|^2$$

$$\times \int_0^T f(z) \exp\left(-2\mathrm{Im}\left(\frac{2\pi}{\lambda} \sqrt{n(\lambda)^2 - \cos^2 \varphi} \right) z \right) \mathrm{d}z, \quad (1)$$

where T represents the implanted substrate thickness and the refractive index n has to be considered for the wavelength of interest λ. The latter corresponds to the wavelength of the incident radiation if the grazing incidence geometry is considered, resp. to the wavelength of an X-ray fluorescence line in the case of the grazing emission geometry. The first factor represents the transmittivity (Fig. 2, bottom middle panel) of the sample surface for the X-ray photons propagating at a grazing angle. The calculation of the GEXRF angular intensity profiles for ion-implanted samples is reported in ref. 26 and can be derived by similar arguments in GIXRF starting from the angular intensity profile for a thick substrate:[63] for ion-implanted samples a weighted depth contribution has to be considered, the weights being given by the dopant distribution. The exponential term in eqn (1) accounts for the absorption of the X-rays propagating at a grazing angle. In case the grazing incidence and emission geometries are combined in the experimental setup, the refraction and absorption of the incident and emitted X-rays has to be considered.[33,34]

The proportionality factor in eqn (1) is determined by the incident (monochromatic) photon flux, the elemental concentration and photoelectric cross-section of the dopant ions, the fluorescence factor and branching ratio for the studied characteristic XRF line as well as the detection efficiency (including X-ray transmission on possible air paths, the solid angle of detection and the detector efficiency). The calculated GEXRF angular intensity profile of the P $K\alpha_1$ line (2013.7 eV) is shown in the bottom right panel, the one for GIXRF (calculated for an incidence of 2200 eV, just above the P K edge at 2145.5 eV) in the bottom left panel of Fig. 2. A direct dependence between the P $K\alpha$ angular intensity profile and the theoretical depth distribution of the implanted P ions can be observed for both grazing XRF techniques. The calculation shows that the angular profiles change gradually with the depth distribution of the implanted ions and that dopant concentration distributions implanted at slightly different implantation energies can be accurately differentiated. For the lowest implantation energies, a large part of the implanted ions are located close to the surface, which explains the observed increase of the intensity at grazing emission angles already below the critical angle. The XRF intensity for grazing angles φ much larger than the critical angle φ_c depends mainly on the implantation dose.

3 Experimental

The investigated ion-implanted samples were single side polished Si and Ge wafers with $\langle 100 \rangle$-orientation, a diameter of 25.4 mm and a thickness of 500 µm. The wafers were doped at the Ion Beam Physics and Materials Research Institute at the Forschungszentrum Dresden-Rossendorf in Germany. The

implantation direction was perpendicular to the wafer surface. The Si wafers were doped with In or Sb ions which were implanted at energies of 1, 2 and 4 keV, respectively, and an implantation fluence of 5×10^{14} atoms per cm^2. The doping with P ions was realized for Si and Ge wafers at a fluence of 5×10^{15} atoms per cm^2 and at energies of 1, 2, 4 and 6 keV, respectively. Additionally a Si wafer was implanted at an energy of 8 keV. The dopant depth distributions were investigated by means of a µ-focus synchrotron radiation based high-energy resolution GEXRF setup. Reported µ-focused GEXRF setups were realized using either a (poly-)capillary optics coupled to an X-ray tube[65–68] or a Kirkpatrick–Baez (KB) mirror system at a synchrotron radiation beam line[69] and using low-energy resolution detection setups.

The In and Sb implantation into Si with 1 keV and the P 4 keV implantation into Ge were additionally analyzed by means of GIXRF using synchrotron radiation.

3.1 GEXRF setup

The depth-profiling measurements by means of micro-focused high energy resolution GEXRF were performed at the ID21 beam line of the European Synchrotron Radiation Facility (ESRF) in Grenoble, France, employing the von Hamos-type bent crystal spectrometer of the University of Fribourg.[70] The grazing emission conditions were realized in the von Hamos spectrometer by decreasing the angle between the sample surface plane and the detection direction defined by the Bragg diffraction angle (at a given diffraction order) for the characteristic XRF line of interest to sufficiently small values (Fig. 3, left panel).[23] The dependence of the intensity of a given XRF line on the grazing emission angle is then assessed by rotating the sample around an axis passing through the sample surface plane and being perpendicular to the spectrometer dispersion plane (defined by the axes on which the crystal and detector are moved when a different characteristic XRF line is to be measured). Moreover, the sample was positioned such that the focused synchrotron radiation beam was incident on the rotation axis. The precision of the sample rotation stage was 0.04 mrad. The focusing of the synchrotron radiation beam was realized with a focusing polycapillary half-lens.[71,72] The compact size of this X-ray optics element permitted its implementation in the spectrometer chamber without modifications of the latter[73] whereas its achromaticity allowed to perform measurements at different synchrotron beam energies without the need for realigning the polycapillary optics.

The synchrotron radiation beam was delivered by the two undulators of the ID21 beam line and the beam size of 3×3 mm^2 was defined by two pairs of slits. Further downstream the synchrotron radiation beam was intercepted by the polycapillary optics which had an entrance aperture of 4.4 mm in diameter. The simultaneous use of two undulators resulted in fluxes as high as 3.5×10^{13} and 2.4×10^{13} ph s^{-1} for the two selected primary beam energies. The experimental measurements with the P-, In- and Sb-implanted Si wafers were performed at an energy of 4240 eV (above the L_3 absorption edge of Sb at 4132 eV), whereas an energy of 3190 eV was selected for the
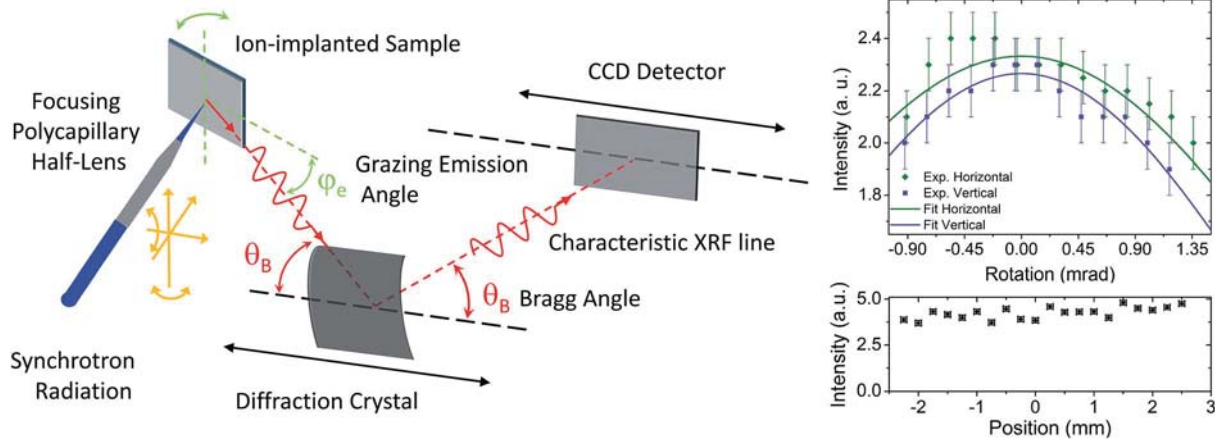
Fig. 3 Schematic representation of the synchrotron radiation based micro-focused high-resolution GEXRF setup (left panel). For the measured characteristic XRF line the grazing emission angles were discriminated by means of the diffraction crystal, the Bragg angle depending on the diffraction crystal and the energy of the characteristic XRF line. The different degrees of freedom for the alignment of the focusing polycapillary half-lens are also shown. For the GEXRF measurements the incidence angle of the synchrotron radiation on the sample was $90° - \theta_B + \varphi_e$. The rotational orientation of the focusing polycapillary optics was crucial to maximize the transmission (top right panel). The micro-focusing option allowed for a laterally resolved scan of the implanted dopant dose at an increased gain (bottom right panel). For the latter measurements the incidence angle of the synchrotron radiation on the sample was set to $90°$.

measurements with the P-implanted Ge wafer in order to diminish the contribution of the photoelectron Bremsstrahlung background in the vicinity of the monitored XRF line. The lower beam energy for the P-implanted Ge wafers was necessary because of the *Z*-dependence of the Bremsstrahlung intensity (originating in the bulk wafer) and the lower L absorption edge of Ge with respect to the K absorption edge of Si. Indeed, the maximum energy of the Bremsstrahlung corresponds to the difference between the primary beam energy and the binding energy of the electrons creating the Bremsstrahlung. Since the Bremsstrahlung intensity decreases with the X-ray energy, the photoelectron Bremsstrahlung background did not affect the measurements of the In and Sb Lα-lines, and only to a small extent the measurements of the P Kα and Si Kα-lines. Moreover, to avoid primary X-ray beam position instabilities, due for example to changes of the thermal load on the beam line optical components, and thus the necessity to realign the focusing polycapillary half-lens, only two X-ray beam energies were used. The monochromatization of the primary beam was realized with two Ni/B$_4$C multilayers, while the higher order harmonics were rejected by Ni mirrors tilted to 7.25 mrad with respect to the incident primary beam. The K resp. L absorption edges of the implanted dopants being all above the K absorption resp. L absorption edges of Si and Ge, the background contribution of the fluorescence lines from the bulk were unavoidable. However, the high energy resolution detection with the von Hamos spectrometer permitted to accurately separate and discriminate the different fluorescence signals. This was of prime importance for the P-implanted Si wafers, the P K$\alpha_{1,2}$-line (2013.7 eV and 2012.7 eV) being separated by about 273 eV from the Si K$\alpha_{1,2}$ line (1739.9 eV). Moreover, the bulk volume contributing to the background signal was limited by the grazing emission conditions.

The implementation of the focusing polycapillary optics (nominal focal spot size of 50 μm) into the von Hamos spectrometer is identical to the solution elaborated in the laboratory where a different polycapillary half-lens is used to focus the collimated Bremsstrahlung emitted by a low-power X-ray tube onto the installed probe.[73] In short, the focusing polycapillary half-lens was installed on a 5-axis positioning stage with 3 translational and 2 rotational movements. For reasons of compactness and accuracy in the rotation alignment the positioning stage was equipped with piezo motors. The translational movements are necessary to position the polycapillary optics in the collimated synchrotron beam and at the focal distance from the sample surface (8 mm for the used polycapillary half-lens). The rotational alignment around the axes transverse to the beam is necessary to maximize the transmission. The sensitivity of the polycapillary optics alignment is shown in Fig. 3 (top right panel), the standard deviation of the transmission curve in the horizontal and vertical directions being 2.1 mrad and 1.7 mrad. The transmitted intensity in the alignment procedure was surveyed by a diode whereas the spot size in the sample plane was surveyed by means of a video system and a fluorescence screen. This approach proved to be sufficiently sensitive to position the focusing polycapillary half-lens at the focal distance from the sample surface. In addition the transmission was measured for the two beam energies used during the experiment by comparing the X-ray fluorescence intensity of the P K$\alpha_{1,2}$ from a P-implanted wafer and of Ge Lα_1 from a Ge wafer with and without the polycapillary optics in the synchrotron radiation beam. The retrieved transmission values were 0.37 ± 0.02 and 0.26 ± 0.02, as compared to values of 0.34 and 0.33 predicted by means of ray-tracing simulations. The photon density gain was, thus, about 10^3. The micro-focusing of the incident X-rays allowed to study the dopant depth profile locally and to perform lateral surface scans with a resolution

6

equal to the focal spot size to characterize the homogeneity of the implanted dose. An example is shown in Fig. 3 (bottom right panel) for a normal incidence angle on the sample. The dopant distribution was found to be quite homogeneously implanted. Note that between GIXRF and GEXRF, only GEXRF allows to profit directly from microsized X-ray beams for laterally resolved measurements. Indeed, in GIXRF the quite large beam footprint on the sample surface has to be considered and spatially resolved measurements parallel to the surface plane require adapted detection setups which are only sensitive to a confined area.[74]

The P Kα$_{1,2}$, In Lα$_1$ (3286.9 eV), Sb Lα$_1$ (3604.7 eV) and Si Kα$_{1,2}$ fluorescence X-ray lines of the P-, In- respectively Sb-implanted Si wafers were diffracted by means of an ADP (101) crystal ($2d = 10.642$ Å) in first order for the P Kα$_{1,2}$ and Si Kα$_{1,2}$ lines, and in second order for the In Lα$_1$ and Sb Lα$_1$ lines. The energy discrimination of the CCD allowed to well separate the Lα$_1$ lines diffracted in second order from the tails of the Si Kα$_{1,2}$ lines diffracted in first order which were partially overlapping on the detector with the dopant fluorescence lines because of similar Bragg diffraction angles. For the P-implanted Ge wafers a TlAP (001) crystal ($2d = 25.772$ Å) was employed in second order for the Ge Lα$_1$ line (1188.0 eV) and the P Kα$_{1,2}$ lines. The diffracted X-rays were detected by means of a back-illuminated position-sensitive CCD camera (1340 × 400 pixels of 20 × 20 μm^2, read-out speed of 1 MHz).

The grazing emission angles were calibrated for each ion-implanted sample by means of the critical angle for the Si Kα$_{1,2}$-line, respectively the Ge Lα$_1$ line. This allowed to determine for each sample the off-set from the reference position of the angular motion. In order to take into account an eventual influence of the dopants on the refractive index of the implanted samples, for each emission line the refractive index of the implanted samples was calculated by taking into account the dopant concentration returned by the SRIM calculation within the extinction depth for grazing angles below the critical angle. The motivation was that the largest refraction of the emitted X-rays takes place at the sample surface so that the sensitivity to the presence of the dopants would be the biggest for this sample region. The changes with respect to a pure wafer were at most on the low percentage level. Moreover, the refractive index was assumed to be depth-independent in order to compute the integral in eqn (1) in a reasonable time interval. The angular intensity profiles $I(\varphi_e)$ were measured at 100 different grazing emission angles φ_e for 50 s per angle for the P Kα$_{1,2}$-line (for both the P-implanted Si and Ge wafers), at 60 different grazing emission angles for 150 s per point for the In and Sb Lα$_1$ lines, and 50 different grazing emission angles for 20 s, respectively 30 s for the Si Kα$_{1,2}$ and Ge Lα$_1$ lines. The points in the angular X-ray fluorescence intensity scans were separated by 0.4 mrad for the dopants (P Kα$_{1,2}$, In Lα$_1$ and Sb Lα$_1$ lines), respectively by 0.8 mrad for the signal from the bulk (Si Kα$_{1,2}$ and Ge Lα$_1$-lines). For reasons of angular resolution, a region of interest (ROI) centered on the maximum intensity at the largest grazing emission angles was defined on the CCD and only the XRF intensity within the ROI was considered in the analysis of the angular intensity scan.[23] The background contribution was estimated from the CCD regions neighboring the defined ROI. Examples of measured GEXRF intensity profiles are displayed in Fig. 4.

3.2 GIXRF setup

The GIXRF measurements were conducted employing the radiometrically calibrated instrumentation of the Physikalisch-Technische Bundesanstalt (PTB) at the electron storage ring BESSY II. An ultrahigh-vacuum (UHV) chamber[22] equipped with calibrated photodiodes to determine the incident photon flux and a calibrated silicon drift detector (SDD) with known spectral response functions and efficiency were used. The known solid angle of detection[75] as well as the use of either tabulated or measured[76] fundamental parameters for the relevant atomic processes, *e.g.*, the photo ionization cross section and the fluorescence yield of the elements of interest allows for a fully reference-free quantitative depth profiling of the implanted element.[49] For the GIXRF experiments, the four-crystal monochromator (FCM) beam line for bending magnet radiation was used.[77]

For means of comparison, the In in Si and Sb in Si 1 keV implantations as well as the P 4 keV implantation in Ge were analyzed with the GIXRF technique. The P implant was measured using a photon energy of 4 keV whereas the In and the Sb implants were both measured using a 5 keV excitation. For each sample, the incidence angle between the sample surface and the incident X-ray beam was varied around the
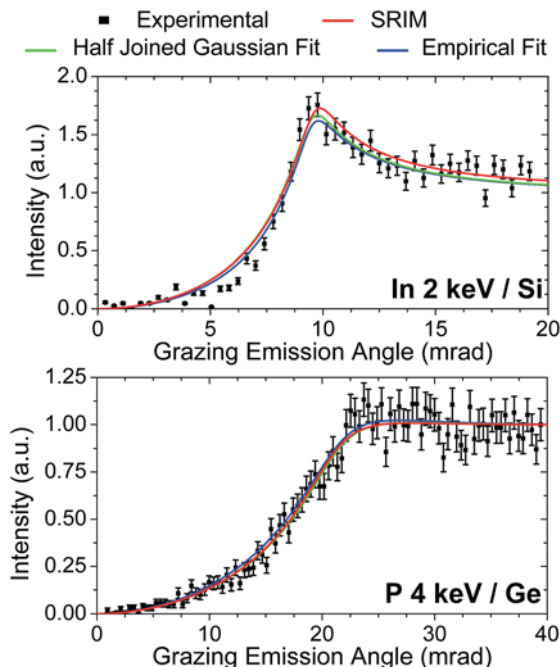

Fig. 4 Examples of GEXRF angular intensity scans for two different ion-implanted samples. The theoretical angular profile obtained by starting from the respective SRIM dependence are also shown, as well as the fitted intensity curves by assuming either an half-joined Gaussian distribution or an empirical approach (further details can be found in the text).

critical angle up to an angle of about 35 mrad. At each angular position a fluorescence spectrum was recorded. The spectra were then deconvoluted using known spectral response functions and relevant background contributions, *e.g.*, Bremsstrahlung from photoelectrons.

The thereby obtained angular fluorescence curves of the implanted elements were modeled using the GIXRF depth profiling technique,[49] employing an IMD[78] calculation of the respective X-ray standing wave field as well as the relevant fundamental parameters to obtain quantitative depth profiles for each implant.

4   Results

4.1   GEXRF

In contrast to SIMS which allows for a more direct measurement, in GEXRF and GIXRF the dopant depth profiles of the ion-implanted samples have to be reconstructed from the experimental angular XRF intensity profile (eqn (1) and Fig. 2). In principle the inversion of eqn (1) would provide an analytical expression of the dopant depth distribution $f(z)$, the only required input being the angular intensity profile $I(\varphi)$ of the XRF signal and the refractive index of the implanted substrate for the energy of interest. As mentioned previously, the dopant concentrations were low enough to consider the refractive index to be depth independent. For higher dopant concentrations, the dependence of the angular intensity profile $I(\varphi)$ on the concentration would be non-linear because of a depth-dependent refractive index. The general inversion of eqn (1) is, however, a severely ill-posed problem.[79] Even if the concentration depth distribution $f(z)$ and the angular intensity profile $I(\varphi)$ are uniquely related to each other, the problem remains ill-posed and a direct inversion of the equation system obtained from a discretization of the grazing angle and the depth z is expected to be highly unstable because of experimental and numerical errors.[25]

Different approaches to invert eqn (1) have been proposed and were successfully applied to synthetic data with very low noise contributions (less than 1%). We will consider hereafter their applicability to the acquired experimental data and point out the difficulties which were encountered. One consists in considering eqn (1) as a truncated Laplace transform.[80] Indeed, the inverse of the Laplace transform operator is mathematically known. However, the inversion is unstable and can not be applied to data with experimental noise unless regularization methods are applied.[80] Even then the sensitivity of the different computation steps to experimental noise introduced too large numerical errors for a successful application to the present experimental GEXRF data. An alternative to the inversion of the truncated Laplace transform is the maximum-entropy method. The inversion of eqn (1) is formulated as a convex constrained optimization problem having a unique solution which converges to the exact depth concentration profile $f(z)$ provided that the noise levels are sufficiently low and enough data points are available.[81] The difficulties with this approach were that the number of points on the grid of the reciprocal space and the extension of the depth region to be considered needed to be well

chosen beforehand. With the maximum entropy method it is also possible to insert some *a priori* assumption about the depth distribution.[81] For the present ion-implanted samples this revealed to be necessary for a successful application of the maximum entropy method. However, the obtained results were found to depend on the *a priori* assumption about the depth distribution.

Moreover the noise levels on the experimental GEXRF angular intensity profiles were found to be too important so that neither one of the inversion approaches could be applied successfully to the acquired data. In addition, the depth distributions of shallow, peaked dopant concentration profiles, *e.g.*, of low energy implantations, are more difficult to reconstruct with the discussed approaches.[80,81] Nevertheless, the inversion of simulated angular intensity profiles can be used in the view of preparing experiments (number of points in the profile, acquisition time).

To determine the dopant depth distribution of the ion-implanted samples, the experimental GEXRF angular intensity profiles acquired were fitted by means of eqn (1). The dopant depth distribution $f(z)$ was replaced by a continuous analytical function, in occurrence a half-joined Gaussian distribution, (a Gaussian distribution where the widths on the left and right side of the center are different). Indeed, the SRIM calculations of the depth distributions for the investigated samples showed that asymmetric dopant depth distributions were to be expected (see Fig. 2 for the case of P-implanted Si wafers). Alternatively, existing tables and functions[82–84] could be used to adjust the depth distribution function $f(z)$ in order to fit the experimental angular intensity profile $I(\varphi)$. The transmittivity and the absorption factor were calculated from the calculated refractive index for the wafer substrate (Fig. 1, right panel), taking the theoretical dopant concentration in the vicinity of the surface into account. The independent free fitting parameters were the center and the widths of the half-joined Gaussian function. This approach was already successfully applied for Al-implanted Si wafers.[48] The analytical expression for and the experimental values of the angular intensity profile were normalized to the same value at a grazing emission angle equal to 40 mrad, thus sufficiently far above the respective critical angles. This allowed to avoid the introduction of an additional fitting parameter, the XRF intensity or equivalently the amplitude of the dopant depth distribution. For quantitative depth profiles acquired with the presented GEXRF setup an accurate instrumental calibration or an adequate calibration sample would be required.

The retrieved dopant depth profiles are compared to the SRIM calculations in Fig. 5 and the numerical results are summarized in Table 1. In overall a good agreement with the SRIM calculations can be observed. The retrieved results for the central peak position match well with the values returned by the SRIM simulation. Except for the P implantations at 4 keV and 8 keV into Si, the values agree within 1 nm, the SRIM values being smaller than the experimentally deduced values, and the agreement improves in general with increasing implantation energies. For the P 4 keV and 8 keV implanted Si wafers, the retrieved peak position of the dopant distribution was about 2 nm below the theoretical value. Also the width of the Gaussian
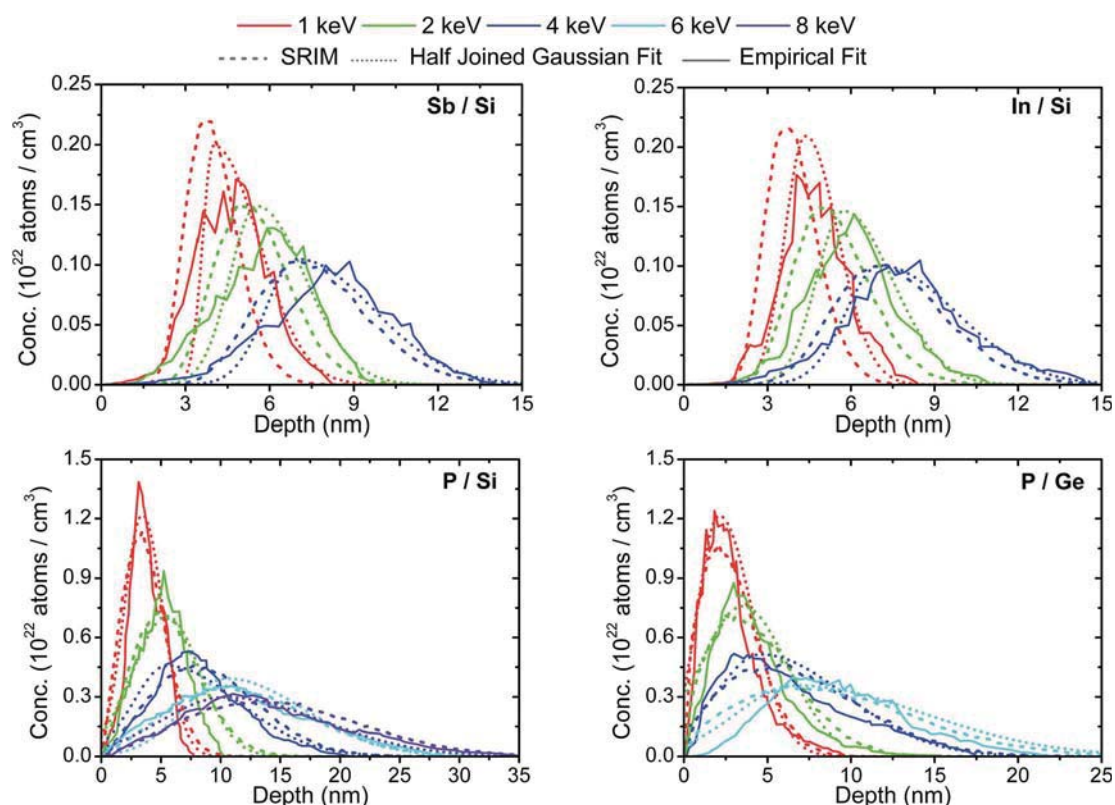
Fig. 5 Comparison of the depth distributions obtained from the angular GEXRF profiles when fitting the experimental data with an analytical expression to describe the dopant depth distribution, in occurrence half-joined Gaussian distributions, to the result of the SRIM simulations. In addition the depth distributions returned by an empirical fitting approach (for details see text and Fig. 6) are shown. All the depth distributions were normalized to the respective nominal implantation dose.

tail extending from the dopant concentration peak towards the sample surface is smaller, in contrast to the other P-implanted samples where a broader first tail than theoretically expected is obtained from the fit. The fitted widths of the Gaussian tail extending from the dopant concentration peak into the bulk volume of the wafer are comparable to the SRIM value or smaller. Thus, the P-implanted Si wafers present, besides a different position of the peak, a slightly different depth

Table 1 Comparison of the results obtained when fitting the GEXRF angular intensity profiles with half-Gaussian functions to the expected depth distributions from SRIM calculations. C stands for the center, W for the width, both in units of nm. The index 1 for the width of the joined half-Gaussian represents the depth region extending from the surface to the center, the index 2 indicates the further depth region. Additionally the evolution predicted by the SRIM calculations of the center and widths of the half-joined Gaussian distribution with the implantation energy allowed to fit the GEXRF angular intensity profiles as a dependence on the implantation energy E (in units of keV). The values in parentheses stand for the standard deviation σ of the results retrieved by the described fitting procedure

Sample	C_{SRIM}	$W_{1,\mathrm{SRIM}}$	$W_{2,\mathrm{SRIM}}$	C_{Fit}	$W_{1,\mathrm{Fit}}$	$W_{2,\mathrm{Fit}}$	E_{Fit}
In 1 keV/Si	3.56	0.69	1.15	4.36 (0.01)	0.74 (0.10)	1.16 (0.15)	1.02 (0.03)
In 2 keV/Si	4.87	1.02	1.66	5.73 (0.01)	0.97 (0.12)	1.75 (0.45)	2.07 (0.07)
In 4 keV/Si	6.80	1.51	2.45	7.03 (0.02)	1.22 (0.55)	2.74 (0.05)	4.15 (0.14)
Sb 1 keV/Si	3.63	0.68	1.14	4.00 (0.35)	0.39 (0.23)	1.61 (0.26)	1.03 (0.03)
Sb 2 keV/Si	4.99	1.04	1.62	5.54 (0.01)	0.97 (0.22)	1.71 (0.22)	2.04 (0.05)
Sb 4 keV/Si	6.88	1.48	2.41	6.98 (0.02)	1.11 (0.55)	2.69 (0.05)	4.03 (0.11)
P 1 keV/Si	3.02	1.42	2.16	3.42 (0.06)	1.52 (0.07)	1.75 (0.01)	1.01 (0.02)
P 2 keV/Si	4.59	2.17	3.40	5.51 (0.14)	2.88 (0.16)	2.77 (0.05)	1.99 (0.03)
P 4 keV/Si	7.36	3.46	5.39	5.48 (0.42)	2.76 (0.38)	5.96 (0.40)	3.99 (0.07)
P 6 keV/Si	9.99	4.60	6.95	10.91 (0.21)	5.47 (0.08)	5.99 (1.10)	6.00 (0.09)
P 8 keV/Si	12.55	5.79	8.60	10.36 (0.48)	5.32 (0.47)	8.07 (0.24)	7.87 (0.17)
P 1 keV/Ge	1.78	1.06	2.37	2.10 (0.03)	1.29 (0.02)	1.99 (0.03)	0.89 (0.03)
P 2 keV/Ge	2.66	1.59	3.63	3.51 (0.11)	2.57 (0.07)	2.69 (0.12)	2.00 (0.04)
P 4 keV/Ge	4.48	2.72	5.48	4.58 (0.14)	2.72 (0.14)	5.04 (0.19)	3.98 (0.09)
P 6 keV/Ge	6.04	3.67	7.16	6.65 (0.55)	3.49 (0.28)	7.67 (0.76)	6.02 (0.14)

evolution than predicted by SRIM calculations. Regarding the P-implantations into Ge, the experimentally deduced depth profiles are shallower than predicted by theory, while the In- and Sb-implantations into Si are found to be broader than the depth distributions calculated by means of SRIM except for the 4 keV implantations. Here the experimental characterization shows a narrower, thus steeper evolution from the surface to the maximum concentration. Nevertheless it can be stated that in general the trends predicted by the SRIM simulations are confirmed.

Assuming that the dependence between the center and widths of the half-joined Gaussian distribution describing the SRIM output and the implantation energy inserted in the calculation is correct, the dopant depth distribution in eqn (1) could as well be described by a single parameter, the implantation energy. This approach proved to be especially useful when fitting GEXRF angular intensity profiles of low-energy Ga implantations in Ge measured with a novel scanning-free setup where the simultaneous contribution of several characteristic XRF lines could not be distinguished because of lacking energy resolution.[52] The fitted implantation energies for the present samples were found to be within a few tens of eV of the nominal implantation energy for all samples except for the In 4 keV Si wafer, the P 8 keV Si wafer and the P 1 keV Ge wafer where the difference between the fitted and nominal values exceeded 100 eV. This difference was, however, in agreement with the observed differences for the fits with 3 independent parameters. While this approach is simple and straightforward, mostly confirming the SRIM simulations for the considered samples, the drawback is that the possible shape of the depth distribution is limited to the predictions of the SRIM calculation.

It should be mentioned that for technologically relevant, annealed samples, where the dopant ions may diffuse during a thermal treatment following the implantation, a different function $f(z)$ than the predicted half-joined Gaussian distribution might have to be used to represent the overall dopant depth distribution. To this end, and as a proof of feasibility, the depth distributions of the ion-implanted were also extracted from the experimental GEXRF angular intensity profiles without assuming, besides a bell-shaped distribution, any *a priori* knowledge of their shape. This iterative fitting approach was presented the first time for Al-implanted Si samples[48] and has been improved in order to be generally applicable to the depth-profiling of any ion-implanted sample by means of grazing XRF techniques.

First, for a given ion-implanted sample, the experimental GEXRF angular intensity distribution was fitted repeatedly, each time with a different discrete distribution from a set of different continuous, polygonal depth functions. The integral in eqn (1) was replaced by a Riemann sum because of the discretized depth distribution function $f(z)$. Each depth function presented a single dopant concentration maximum and was discretized with regularly spaced points. The goal was to select from the pre-defined set the distribution with which the experimental GEXRF data of the considered sample are best fitted. In contrast to the former approach this step makes the approach much less sensitive to the actual shape of the distribution in the depth

direction. This first step allows also to estimate the extension of the dopant distribution in the depth direction. Once the most suitable distribution was chosen, the depth coordinates z_i and the concentration values $f(z_i)$ $(i = 1, …, p)$ of the p points of the selected distribution were allowed to vary within square boundary limits to further improve the fit of the experimental grazing emission profile. The boundary limits were fixed on the depth axis by the depth resolution (obtained from the depth region over which the selected distribution extends and the number of points p) and on the concentration axis by the initial concentration value and the average absolute value of the slope between the different points in the depth distribution. The iteration process was then started with a smoothed spline interpolation of the obtained set of point coordinates $(z_i, f(z_i))$. The smoothing was necessary to attenuate eventual spikes in the depth distribution curve, a problem which was less pronounced when fitting symmetric depth profiles (for example Al implantations are well described by Gaussian distributions) or when the depth distribution spread over a larger depth range (higher implantation energies). In each iteration step the depth resolution was improved by increasing the number of regularly spaced points p in the depth distribution curve and the GEXRF intensity profile was fitted with the discretized version of eqn (1) to obtain a new dopant depth distribution (Fig. 6). The starting
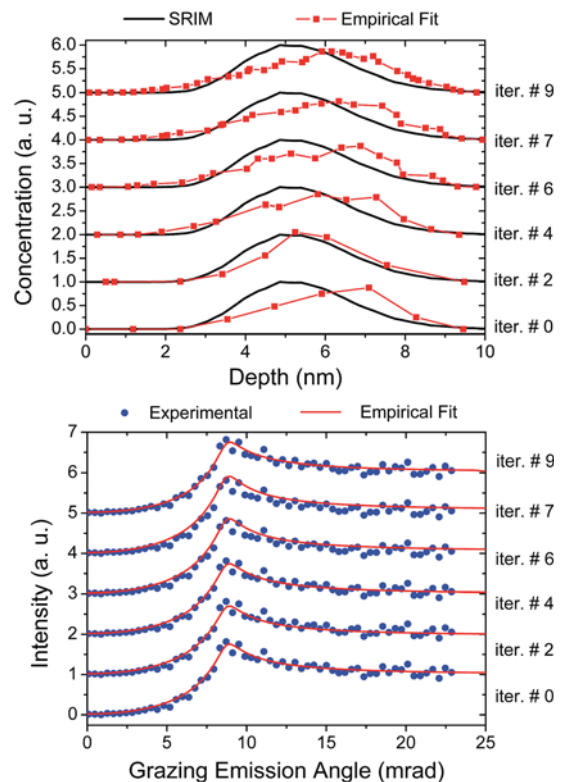

Fig. 6 Illustration of the empirical iterative fitting approach. Starting from a polygonal depth distribution which best fitted the GEXRF angular intensity profile, the depth resolution in the dopant distribution is increased in each iterative step by using an increased number of points on the discretized depth scale. More details can be found in the text.

10

values of the new set of regularly spaced point coordinates (z_i, $f(z_i)$) were determined from the interpolation curve of the depth coordinate values returned by the previous iteration step. The boundary limits of the individual points were defined as explained for the step preceding the iterative procedure. At the end of each iteration step neighboring points which were too close to each other (compared to the depth resolution of the actual iteration step) were replaced by a single point. If the concentration value of the last point in the depth distribution (z_i, $f(z_i)$) was too important compared to the maximum concentration value, an additional point at a larger depth with a lower, extrapolated concentration value was added. The iteration process was stopped when the desired depth resolution was obtained.

After successfully testing this approach with synthetic data, it was applied to the experimentally acquired GEXRF profiles. The results are plotted in Fig. 5 together with the results obtained when fitting the experimental data with the half-joined Gaussian distribution. In general the depth position of the peak concentrations predicted by both fitting approaches are close together as well as the depth range over which the depth distributions extend. The shapes of the distributions do not match as closely but do not contradict neither the trends of the SRIM calculation nor of the results retrieved by the fits with half-joined Gaussian distributions. As a cross-check and validation tool on experimental data when selecting the depth distribution function $f(z)$ with which the GEXRF will be fitted this approach might be very helpful in addition to the SRIM simulations.

4.2 GIXRF

For validation purposes, selected samples were also analyzed with the GIXRF approach using absolutely calibrated instrumentation.[22] This allowed to extract both the dopant depth distribution and the total implanted dose. The depth distributions obtained by means of GIXRF for the In and Sb 1 keV implantations into Si and the P 4 keV implantation into Ge are shown in Fig. 7 together with the respective GEXRF and SRIM results. For the latter sample the depth distributions are congruent with each other and only minor differences in the depth distribution curves can be observed. Also the experimental quantification of GIXRF agrees quite well with the nominal implantation dose to which SRIM and GEXRF were normalized to. For the In and Sb 1 keV implantations into Si, the GIXRF results reproduce the SRIM data in terms of the peak position in the dopant concentration distribution, presenting thus the same difference of 0.4, respectively 0.8 nm as the SRIM simulation with respect to GEXRF. One possible reason for the observed shift in GEXRF could be that the refractive index at the refracting surface was somewhat different than the theoretical value due to the influence of the implant. Indeed, GIXRF suffers from the same limitation of the accurate knowledge on the optical constants as GEXRF. This has already been experienced for Al-implanted Si wafers.[49] Moreover, the GEXRF calibration procedure with the Si K$\alpha_{1,2}$ lines could be affected as well for the same reason. This underlines the importance of an accurate
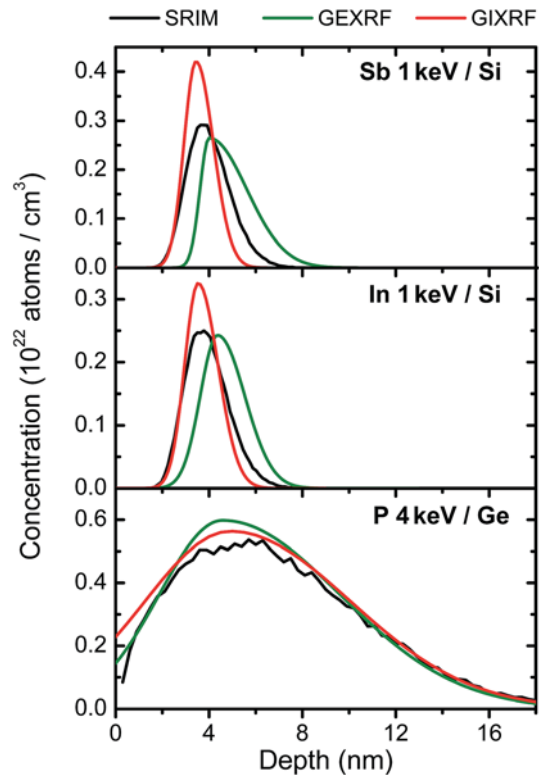

Fig. 7 Comparison of the dopant depth distributions retrieved by means of GEXRF, GIXRF and SRIM for the In and Sb 1 keV implantations into Si and the P 4 keV implantation into Ge. Additionally the output of the SRIM simulation is shown. The SRIM and GEXRF results are normalized for the nominal implantation dose while the reference-free GIXRF results reflect the experimentally quantified implantation dose.

knowledge of the refractive index. X-ray reflectometry (XRR) measurements at the energy of interest allow for an experimental assessment of the refractive index at the energy of interest.[47] The joint use of complementary XRR and grazing XRF data can be used to provide a more complete description of the sample[85] in order to further improve the XRF depth profiling results. For higher implantation energies the difference between GEXRF and SRIM was less important since the dopant concentration within the first few nanometers below the surface was smaller and the overall dopant distribution wider. The effect of the dopants on the effective refractive index is diminished. For other dopant–substrate combinations the refractive index of the dopant and substrate atoms for the considered energies of interest were closer together and the effect of the dopant atoms on the bulk refractive index was therefore less important.

Regarding the shape of the dopant depth distribution, the GIXRF results exhibit on the other hand for the In and Sb 1 keV implantations into Si shallower depth distributions. Especially the tail extending from the concentration maximum into the bulk is steeper. The 1 keV In and Sb implants represent therefore a limiting case with regard to reliable depth-profiling measurements with grazing XRF techniques because of the discussed uncertainties with regard to the exact values of the

optical constants. It has also to be considered that for the lowest implantation energies a depth-dependent variation of the refractive index might have to be taken into account because of the high local dopant concentrations. In this case a possible alternative depth-profiling algorithm without having to solve the integral in eqn (1) would be to treat an ion-implanted sample as a virtual multilayer stack, each layer in the stack being characterized by a different refractive index in agreement with the dopant concentration in the respective layer. Multilayer structures can be treated in GIXRF with the IMD software,[78] in the case of GEXRF an analytic formula can be found in the literature.[79] The multilayer approach could be implemented, analogous to the presented empirical approach, in an iterative algorithm in which one can start with only a few layers and adjust the concentration when fitting the angular profile, then increase the number of layers and recalculate the refractive index in each layer in-between the iteration steps. Also the boundaries on the concentration values in the fit in each iteration step could be set by means of a confidence interval on the Gaussian or half-joined Gaussian distribution imposed on the depth dependence (or layer-to-layer evolution) of the dopant concentration values. The latter aspect can be realized by fitting the variation of concentration values through the different layers, *i.e.*, the depth distribution of the dopant concentration, with the selected analytical function for the dopant depth dependence. Since the fitting parameter are concentration values, this approach can potentially provide quantitative results.

5 Conclusions & outlook

Synchrotron radiation based grazing XRF techniques present a great potential for the accurate, nanometer-scale characterization of shallow in-depth distributions of dopants implanted with energies of only a few keV (ultra-low energy ion implantations) in Si and Ge wafers. Both, GEXRF and GIXRF, allow to extend the accessibility of depth-profiling metrology measurements towards nanoscale dopant distributions with depth scales relevant for technological applications without requiring reference samples and without suffering from the limits of particle based methods, *i.e.*, the maximum accessible depth range of electron-based methods or the transient effects of sputter-based approaches. Calibrations samples would only be required for quantification issues if the used setup does not provide absolute results. The pronounced dependence of the GEXRF and GIXRF intensity profiles on the implantation energy for a given dopant–substrate combination allows to precisely distinguish between different dopant depth distributions. The limitations with respect to the ion-implanted wafers which can be investigated are in principle given by the depth range to which the setup is sensitive at the largest grazing angle, the knowledge of the refractive index for the energy of interest and the implanted dose. For the investigated samples the dopant concentrations were sufficiently low to use a depth-independent refractive index which was calculated from the tabulated values for the wafer and dopant elements for the energy of interest. Because of the implantation dose and the shallow region to be

doped, the samples with the lowest implantation energies represented a limiting case for a reliable investigation of the depth-profiles by means of the presented approaches to analyze the grazing XRF profiles. In these cases the refractive index has to be experimentally assessed by means of XRR, a technique which can be conveniently combined with a GIXRF setup.[85] Also further investigations assessing the limits towards the local dopant concentration by varying for the lowest implantation energy the implantation dose are called for. A route for improvement in the future could be, besides an inclusion of XRR for a more accurate experimental knowledge of the optical constants, to use an iterative approach for the depth-dependent treatment of the refractive index in order to obtain more reliable results. For larger implantation energies, the agreement with the theoretical predictions improved as the dopant profile extended over larger regions and the local dopant concentration decreased.

The used GEXRF setup represents a novel and unique, yet versatile combination of micro-focused XRF excitation (increased gain), high-energy resolution XRF detection (better background rejection capabilities and increased signal-to-noise ratio) and the grazing emission geometry. The angular resolution is ensured by the dispersive element and the spatially resolved XRF detection, while the laterally resolved XRF excitation of the sample together with nanometer-resolution depth-profiling of GEXRF makes an elemental three-dimensional sample study conceivable. In combination with a scanning-free GEXRF arrangement[52] only the lateral dimensions would have to be scanned. From the experimental GEXRF intensity profiles the dopant depth distributions could be accurately reconstructed using an analytical approach and were found to be in a fair agreement with the results from the SRIM simulation, except for the In and Sb 1 keV implantations into Si. These results were also confirmed for some samples with the help of the radiometrically calibrated GIXRF setup of the PTB which furthermore delivered quantitative results. The experimental GEXRF intensity profiles were also fitted by using an iterative fitting algorithm in which only a bell-shaped depth distribution function is assumed without defining the exact shape of it. This empirical approach can be applied towards thermally treated samples or towards diffusion process samples.

References

1 C. B. Yarling, *J. Vac. Sci. Technol., A*, 2000, **18**, 1746–1750.
2 J. M. Poate and L. Rubin, *Ind. Phys.*, 2003, **9**, 12–15.
3 K. Suzuki, R. Sudo, Y. Tada, M. Tomotani, T. Feudel and W. Fichtner, *Solid-State Electron.*, 1998, **42**, 1671–1678.
4 H. Wu, N. Conrad, W. Luo and P. D. Ye, *Electron Devices Meeting (IEDM)*, IEEE International, 2014, pp. 9.3.1–9.3.4.

5 G. Scappucci, G. Capellini, W. M. Klesse and M. Y. Simmons, *Nanoscale*, 2013, **5**, 2600–2615.

6 Q. Xie, S. Deng, M. Schaekers, D. Lin, M. Caymax, A. Delabie, X.-P. Qu, Y.-L. Jiang, D. Deduytsche and C. Detavernier, *Semicond. Sci. Technol.*, 2012, **27**, 074012.

7 R. Pillarisetty, *Nature*, 2011, **479**, 324–328.

8 H.-Y. Yu, Y. Nishi, K. Saraswat, S.-L. Cheng and P. Griffin, *IEEE Electron Device Lett.*, 2009, **30**, 1002–1004.

9 H. Bracht, S. Schneider, J. N. Klug, C. Y. Liao, J. L. Hansen, E. E. Haller, A. N. Larsen, D. Bougeard, M. Posselt and C. Wündisch, *Phys. Rev. Lett.*, 2009, **103**, 255501.

10 C. Wündisch, M. Posselt, B. Schmidt, V. Heera, T. Schumann, A. Mücklich, R. Grötzschel, W. Skorupa, T. Clarysse, E. Simoen and H. Hortenbach, *Appl. Phys. Lett.*, 2009, **95**, 252107.

11 C. O. Chui, K. Gopalakrishnan, P. B. Griffin, J. D. Plummer and K. C. Saraswat, *Appl. Phys. Lett.*, 2003, **83**, 3275–3277.

12 R. N. S. Sodhi, *Analyst*, 2004, **129**, 483–487.

13 W. Chu and J. Liu, *Mater. Chem. Phys.*, 1996, **46**, 183–188.

14 M. Copel, *IBM J. Res. Dev.*, 2000, **44**, 571–582.

15 G. Boudreault, R. Elliman, R. Grötzschel, S. Gujrathi, C. Jeynes, W. Lennard, E. Rauhala, T. Sajavaara, H. Timmers, Y. Wang and T. Weijers, *Nucl. Instrum. Methods Phys. Res., Sect. B*, 2004, **222**, 547–566.

16 R. Klockenkämper, H. Krzyzanowska and A. von Bohlen, *Surf. Interface Anal.*, 2003, **35**, 829–834.

17 I. Holfelder, B. Beckhoff, R. Fliegauf, P. Hönicke, A. Nutsch, P. Petrik, G. Roeder and J. Weser, *J. Anal. At. Spectrom.*, 2013, **28**, 549–557.

18 D. Abou-Ras, R. Caballero, C.-H. Fischer, C. Kaufmann, I. Lauermann, R. Mainz, H. Mönig, A. Schöpke, C. Stephan, C. Streeck, S. Schorr, A. Eicke, M. Döbeli, B. Gade, J. Hinrichs, T. Nunney, H. Dijkstra, V. Hoffmann, D. Klemm, V. Efimova, A. Bergmaier, G. Dollinger, T. Wirth, W. Unger, A. Rockett, A. Perez-Rodriguez, J. Alvarez-Garcia, V. Izquierdo-Roca, T. Schmid, P.-P. Choi, M. Müller, F. Bertram, J. Christen, H. Khatri, R. Collins, S. Marsillac and I. Kötschau, *Microsc. Microanal.*, 2011, **17**, 728–751.

19 C. E. I. Dos Santos, S. M. Shubeita, L. Amaral, P. L. Grande and J. F. Dias, *X-Ray Spectrom.*, 2011, **40**, 157–161.

20 R. Escobar Galindo, R. Gago, D. Duday and C. Palacio, *Anal. Bioanal. Chem.*, 2010, **396**, 2725–2740.

21 J. Wang, U. Starke and E. Mittemeijer, *Thin Solid Films*, 2009, **517**, 3402–3407.

22 B. Beckhoff, *J. Anal. At. Spectrom.*, 2008, **23**, 845–853.

23 Y. Kayser, J. Szlachetko, D. Banaś, W. Cao, J.-Cl. Dousse, J. Hoszowska, A. Kubala-Kukuś and M. Pajek, *Spectrochim. Acta, Part B*, 2013, **88**, 136–149.

24 M. Claes, P. de Bokx and R. Van Grieken, *X-Ray Spectrom.*, 1999, **28**, 224–229.

25 P. de Bokx, C. Kok, A. Bailleul, G. Wiener and H. Urbach, *Spectrochim. Acta, Part B*, 1997, **52**, 829–840.

26 H. P. Urbach and P. K. de Bokx, *Phys. Rev. B: Condens. Matter Mater. Phys.*, 1996, **53**, 3752–3763.

27 N. Alov, *Inorg. Mater.*, 2011, **47**, 1487–1499.

28 F. Meirer, A. Singh, P. Pianetta, G. Pepponi, F. Meirer, C. Streli and T. Homma, *TrAC, Trends Anal. Chem.*, 2010, **29**, 479–496.

29 A. von Bohlen, *Spectrochim. Acta, Part B*, 2009, **64**, 821–832.

30 P. Wobrauschek, *X-Ray Spectrom.*, 2007, **36**, 289–300.

31 K. N. Stoev and K. Sakurai, *Spectrochim. Acta, Part B*, 1999, **54**, 41–82.

32 Y. C. Sasaki and K. Hirokawa, *Appl. Phys. Lett.*, 1991, **58**, 1384–1386.

33 K. Tsuji and K. Hirokawa, *Spectrochim. Acta, Part B*, 1993, **48**, 1471–1480.

34 K. Tsuji and K. Hirokawa, *J. Appl. Phys.*, 1994, **75**, 7189–7194.

35 K. Tsuji, S. Sato and K. Hirokawa, *Rev. Sci. Instrum.*, 1995, **66**, 4847–4852.

36 S. Sato, K. Tsuji and K. Hirokawa, *Appl. Phys. A*, 1996, **62**, 87–93.

37 J. Szlachetko, D. Banaś, A. Kubala-Kukuś, M. Pajek, W. Cao, J.-Cl. Dousse, J. Hoszowska, Y. Kayser, M. Szlachetko, M. Kavčič, M. Salome and J. Susini, *J. Appl. Phys.*, 2009, **105**, 086101.

38 A. Kubala-Kukuś, D. Banaś, W. Cao, J.-Cl. Dousse, J. Hoszowska, Y. Kayser, M. Pajek, M. Salomé, J. Susini, J. Szlachetko and M. Szlachetko, *Phys. Rev. B: Condens. Matter Mater. Phys.*, 2009, **80**, 113305.

39 Z. M. Spolnik, M. Claes, R. E. Van Grieken, P. K. de Bokx and H. P. Urbach, *Spectrochim. Acta, Part B*, 1999, **54**, 1525–1537.

40 S. de Gendt, K. Kenis, M. Baeyens, P. Mertens, M. Heyns, G. Wiener, S. Kidd, D. Knotter and P. de Bokx, *Mater. Res. Soc. Symp. Proc.*, 1997, **477**, 397–402.

41 D. Hellin, S. D. Gendt, N. Valckx, P. W. Mertens and C. Vinckier, *Spectrochim. Acta, Part B*, 2006, **61**, 496–514.

42 C. Streli, G. Pepponi, P. Wobrauschek, N. Zöger, P. Pianetta, K. Baur, S. Pahlke, L. Fabry, C. Mantler, B. K. ßer and W. Malzer, *Spectrochim. Acta, Part B*, 2003, **58**, 2105–2112.

43 S. Pahlke, *Spectrochim. Acta, Part B*, 2003, **58**, 2025–2038.

44 K. Baur, S. Brennan, P. Pianetta and R. Opila, *Anal. Chem.*, 2002, **74**, 608A–616A.

45 R. S. Becker, J. A. Golovchenko and J. R. Patel, *Phys. Rev. Lett.*, 1983, **50**, 153–156.

46 D. Ingerle, F. Meirer, G. Pepponi, E. Demenev, D. Giubertoni, P. Wobrauschek and C. Streli, *Spectrochim. Acta, Part B*, 2014, **99**, 121–128.

47 P. Hönicke, Y. Kayser, B. Beckhoff, M. Muller, J.-Cl. Dousse, J. Hoszowska and S. H. Nowak, *J. Anal. At. Spectrom.*, 2012, **27**, 1432–1438.

48 Y. Kayser, D. Banaś, W. Cao, J.-Cl. Dousse, J. Hoszowska, P. Jagodziński, M. Kavčič, A. Kubala-Kukuś, S. Nowak, M. Pajek and J. Szlachetko, *X-Ray Spectrom.*, 2012, **41**, 98–104.

49 P. Hönicke, B. Beckhoff, M. Kolbe, D. Giubertoni, J. van den Berg and G. Pepponi, *Anal. Bioanal. Chem.*, 2010, **396**, 2825–2832.

50 G. Pepponi, D. Giubertoni, M. Bersani, F. Meirer, D. Ingerle, G. Steinhauser, C. Streli, P. Hönicke and B. Beckhoff, *J. Vac. Sci. Technol. B*, 2010, **28**, C1C59–C1C64.

51 D. Giubertoni, E. Iacob, P. Hönicke, B. Beckhoff, G. Pepponi, S. Gennaro and M. Bersani, *J. Vac. Sci. Technol., B:*

Microelectron. Nanometer Struct.–Process., Meas., Phenom., 2010, **28**, C1C84–C1C89.

52 Y. Kayser, J. Szlachetko and J. Sá, *Rev. Sci. Instrum.*, 2013, **84**, 123102.

53 I. Koshelev, A. Paulikas, M. Beno, G. Jennings, J. Linton, M. Grimsditch, S. Uran and B. Veal, *Oxid. Met.*, 2007, **68**(15), 37–51.

54 M. L. Monaghan, T. Nigam, M. Houssa, S. D. Gendt, H. P. Urbach and P. K. de Bokx, *Thin Solid Films*, 2000, **359**, 197–202.

55 K. Tsuji, H. Takenaka, K. Wagatsuma, P. K. de Bokx and R. Van Grieken, *Spectrochim. Acta, Part B*, 1999, **54**, 1881–1888.

56 M. Müller, P. Hönicke, B. Detlefs and C. Fleischmann, *Materials*, 2014, **7**, 3147–3159.

57 B. Pollakowski, P. Hoffmann, M. Kosinova, O. Baake, V. Trunova, R. Unterumsberger, W. Ensinger and B. Beckhoff, *Anal. Chem.*, 2013, **85**, 193–200.

58 R. Unterumsberger, B. Pollakowski, M. Müller and B. Beckhoff, *Anal. Chem.*, 2011, **83**, 8623–8628.

59 H. J. Sánchez and C. A. Pérez, *Spectrochim. Acta, Part B*, 2010, **65**, 466–470.

60 S. H. Nowak, D. Banaś, W. Błachucki, W. Cao, J.-Cl. Dousse, P. Hönicke, J. Hoszowska, Ł. Jabłoński, Y. Kayser, A. Kubala-Kukuś, M. Pajek, F. Reinhardt, A. Savu and J. Szlachetko, *Spectrochim. Acta, Part B*, 2014, **98**, 65–75.

61 F. Reinhardt, S. H. Nowak, B. Beckhoff, J.-Cl. Dousse and M. Schoengen, *J. Anal. At. Spectrom.*, 2014, **29**, 1778–1784.

62 F. Reinhardt, J. Osan, S. Torok, A. E. Pap, M. Kolbe and B. Beckhoff, *J. Anal. At. Spectrom.*, 2012, **27**, 248–255.

63 R. Klockenkämper, *Total Reflection X-ray Fluorescence Analysis*, Wiley-Interscience, 1996, vol. 140.

64 J. F. Ziegler, *Nucl. Instrum. Methods Phys. Res., Sect. B*, 2004, **219–220**, 1027–1036.

65 J. Yang, K. Tsuji, X. Lin, D. Han and X. Ding, *Thin Solid Films*, 2009, **517**, 3357–3361.

66 T. Awane, S. Fukuoka, K. Nakamachi and K. Tsuji, *Anal. Chem.*, 2009, **81**, 3356–3364.

67 T. Emoto, Y. Sato, Y. Konishi, X. Ding and K. Tsuji, *Spectrochim. Acta, Part B*, 2004, **59**, 1291–1294.

68 K. Tsuji and F. Delalieux, *Spectrochim. Acta, Part B*, 2003, **58**, 2233–2238.

69 T. Noma and A. Iida, *Rev. Sci. Instrum.*, 1994, **65**, 837–844.

70 J. Hoszowska, J.-Cl. Dousse, J. Kern and C. Rhême, *Nucl. Instrum. Methods Phys. Res., Sect. A*, 1996, **376**, 129–138.

71 C. A. MacDonald, *X-Ray Opt. Instrum.*, 2010, **2010**, 17.

72 P. J. Schields, D. M. Gibson, W. M. Gibson, N. Gao, H. Huang and I. Y. Ponomarev, *Powder Diffr.*, 2002, **17**, 70–80.

73 Y. Kayser, W. Błachucki, J.-Cl. Dousse, J. Hoszowska, M. Neff and V. Romano, *Rev. Sci. Instrum.*, 2014, **85**, 043101.

74 A. Kühn, O. Scharf, I. Ordavo, H. Riesemeier, U. Reinholz, M. Radtke, A. Berger, M. Ostermann and U. Panne, *J. Anal. At. Spectrom.*, 2011, **26**, 1986–1989.

75 B. Beckhoff, R. Fliegauf, M. Kolbe, M. Müller, J. Weser and G. Ulm, *Anal. Chem.*, 2007, **79**, 7873–7882.

76 M. Kolbe, P. Hönicke, M. Müller and B. Beckhoff, *Phys. Rev. A*, 2012, **86**, 042512.

77 M. Krumrey and G. Ulm, *Nucl. Instrum. Methods Phys. Res., Sect. A*, 2001, **467–468**, 1175–1178.

78 D. L. Windt, *Comput. Phys.*, 1998, **12**, 360–370.

79 H. P. Urbach and P. K. de Bokx, *Phys. Rev. B: Condens. Matter Mater. Phys.*, 2001, **63**, 085408.

80 C. Kok and H. P. Urbach, *Inverse Probl. Eng.*, 1999, **7**, 433–470.

81 S. M. P. Smolders and H. P. Urbach, *J. Eng. Math.*, 2002, **43**, 115–134.

82 H. Zhang, M. Gao, L. Xu, M. Lin, X. Niu and W. Lv, *Solid State Ionics*, 2008, **179**, 832–836.

83 K. Suzuki, K. Ikeda, Y. Yamashita, M. Harada, N. Taoka, O. Kiso, T. Yamamoto, N. Sugiyama and S.-I. Takagi, *IEEE Trans. Electron Devices*, 2009, **56**, 627–633.

84 K. Suzuki and R. Sudo, *Solid-State Electron.*, 2000, **44**, 2253–2257.

85 A. J. G. Leenaers and D. K. G. de Boer, *X-Ray Spectrom.*, 1997, **26**, 115–121.